PNAS RESEARCH ARTICLE | EARTH, ATMOSPHERIC, AND PLANETARY SCIENCES
SUSTAINABILITY SCIENCE

Historical Southern Hemisphere biomass burning variability inferred from ice core carbon monoxide records

Ivo Strawson[a,b,1], Xavier Faïn[c], Thomas K. Bauska[b], Francesco Muschitiello[d,e], Diana O. Vladimirova[b], Dieter R. Tetzner[b], Jack Humby[b], Elizabeth R. Thomas[b], Pengfei Liu[f], Bingqing Zhang[f], Roberto Grilli[c], and Rachael H. Rhodes[a,1]

Affiliations are included on p. 7.

Edited by Mark Thiemens, University of California San Diego, La Jolla, CA; received February 16, 2024; accepted June 10, 2024

Biomass burning plays an important role in climate-forcing and atmospheric chemistry. The drivers of fire activity over the past two centuries, however, are hotly debated and fueled by poor constraints on the magnitude and trends of preindustrial fire regimes. As a powerful tracer of biomass burning, reconstructions of paleoatmospheric carbon monoxide (CO) can provide valuable information on the evolution of fire activity across the preindustrial to industrial transition. Here too, however, significant disagreements between existing CO records currently allow for opposing fire histories. In this study, we reconstruct a continuous record of Antarctic ice core CO between 1821 and 1995 CE to overlap with direct atmospheric observations. Our record indicates that the Southern Hemisphere CO burden ([CO]) increased by 50% from a preindustrial mixing ratio of ca. 35 ppb to ca. 53 ppb by 1995 CE with more variability than allowed for by state-of-the-art chemistry-climate models, suggesting that historic CO dynamics have been not fully accounted for. Using a 6-troposphere box model, a 40 to 50% decrease in Southern Hemisphere biomass-burning emissions, coincident with unprecedented rates of early 20th century anthropogenic land-use change, is identified as a strong candidate for this mismatch.

carbon monoxide | ice cores | Southern Hemisphere | preindustrial | biomass burning

Significance

The role humans may have played in altering land cover and disrupting the carbon cycle with fire is hotly debated. As biomass burning is a major source of atmospheric carbon monoxide (CO), information on past CO variability is valuable for paleofire studies. This study presents high-resolution records of CO measured in air trapped as bubbles in Antarctic ice. During the early 20th century, Southern Hemisphere atmospheric CO increased less than expected based on current emissions inventories. This suggests that fire activity likely decreased during this period in line with rapid rates of Southern Hemisphere land-use change.

Biomass burning impacts terrestrial carbon cycling, atmospheric greenhouse gas and aerosol burdens, atmospheric chemistry, and ultimately climate forcing (1). Significant disagreement in modeled wildfire evolution since the preindustrial (here, 1850 CE) (2), however, has so far limited our understanding of the role biomass burning has played in recent climate change (3). Primarily, model discrepancies reflect the uncertain magnitude of fire activity in the preindustrial relative to present day (4–6), and in turn, how to realistically implement the response of biomass burning to human-driven changes in land-use and fire suppression/ignition during a period of sustained population growth and societal development (1, 2, 5, 7–10). Accurate fire modeling in support state-of-the-art climate reconstructions (11, 12) therefore requires reliable paleofire proxy data against which to test predictions.

Over the past millennium, significant spatiotemporal variability in biomass burning has been inferred from ice core trace gas (13–20) and impurity records (21–24), regional and global compilations of sedimentary charcoal (25, 26), and tree fire-scaring records (27, 28). While these archives are generally coherent in suggesting biomass burning was high during the 1400s before declining toward a minimum in the 1600s, large discrepancies exist among records of the past 200 y. Global charcoal records (e.g., 25), for example, suggest biomass burning increased from a minimum in 1700 CE to a peak in the late 19th century at up to 4 times modern levels before declining throughout the 1900s. Conversely, ice core trace gas records of ethane (17), acetylene (18) and the stable isotope composition of methane (δ^{13}C-CH_4) (e.g., 13), all suggest biomass burning remained at historically low levels until at least 1850 CE. Antarctic records of the short-lived acetylene (18) have then been suggested to demonstrate a gradual increase in Southern Hemisphere biomass burning throughout the early 20th century.

As the major reactive trace gas emitted from fire (29), paleoatmospheric records of ice core carbon monoxide (CO) are crucial to constraining a consistent paleofire history (5). Today, direct emissions of CO from the combustion of biomass and fossil fuels account for roughly half of the atmospheric CO burden ([CO])—the bulk of the remainder produced from the secondary photochemical oxidation of CH_4 and nonmethane hydrocarbons (NMHCs) (30, 31). Oxidation by hydroxyl radicals (OH) accounts for over 90% of the CO sink (30). The preindustrial CO budget was comparatively simpler, whereby negligible anthropogenic fossil fuel emissions and

Author contributions: I.S., E.R.T., and R.H.R. designed research; I.S., D.O.V., D.R.T., J.H., and E.R.T. performed research; I.S. analyzed data; X.F. and R.G. provided analytical expertise and instrumentation; T.K.B. built the box model; F.M. provided expertise in numerical methods; P.L. and B.Z. contributed additional model outputs; and I.S., X.F., T.K.B., and R.H.R. wrote the paper.

The authors declare no competing interest.

This article is a PNAS Direct Submission.

[1]To whom correspondence may be addressed. Email: is499@cam.ac.uk or rhr34@cam.ac.uk.

This article contains supporting information online at https://www.pnas.org/lookup/suppl/doi:10.1073/pnas.2402868121/-/DCSupplemental.

Published August 5, 2024.

a relatively stable CH_4 burden (32) would have made fire activity the primary control on atmospheric CO variability. Interhemispheric mixing of CO, however, is restricted by its relatively short mean atmospheric lifetime of around 2 mo (33), meaning Greenland and Antarctic ice cores histories must be constructed separately (e.g., 20, 34).

Despite their potential utility, existing Antarctic ice core CO records currently allow for opposing histories of preindustrial biomass burning (15, 20). Faïn et al. (20), for example, have recently argued that Antarctic CO data from Vostok (35), D47 (15, 35), South Pole (35), and Law Dome (13) are likely impacted by large unaccounted blanks and should not be taken as support for a late 19th century peak in Southern Hemisphere biomass burning, as argued by Wang et al. (15). Instead, the CO mixing ratios reported by Faïn et al. (20) are more consistent with other ice short-lived ice core trace gas histories (19) in suggesting biomass burning remained low in the lead up to the turn of the 20th century. New records are therefore required to reconcile current disagreements before they can be confidently used as model benchmarks. Furthermore, the typically slow process by which air is trapped in bubbles of Antarctic ice has so far restricted the modern extent of ice core CO records to the late 19th century. Previous studies, notably also by Faïn et al. (20) but also Assonov et al. (36), have utilized inverse reconstructions of [CO] constrained by measurements of air pumped from the porous firn layer of the Antarctic ice sheet to bridge the gap to the onset of direct atmospheric observations. These firn air reconstructions suggest CO increased from 1900 CE toward a peak in the early 1990s with a brief interruption to growth in the mid-20th century, but it is noteworthy that these inversions are reliant on low temporally resolved measurement constraints.

Here, we use three high snow accumulation rate (>440 kg m^{-2} y^{-1}) ice cores to reconstruct Antarctic [CO] from 1821 to 1995 CE. By selecting locations with high snowfall rates, and therefore relatively rapid rates of air bubble closure, we achieve an overlap between the ice core air and the onset of direct atmospheric observations without the need for firn air inversions. Furthermore, the fast rates of bubble trapping at our sites limit diffusive mixing of the air within the firn column, meaning that air trapped in the bubbles has a relatively narrow gas age distribution (37), allowing us to resolve multidecadal scale variations in [CO] since the preindustrial. Using an atmospheric box model, we then demonstrate that Southern Hemisphere biomass burning was likely more variable than allowed by the fire inventories currently driving state-of-the-art chemistry-climate models (CCMs).

Results

Ice Core Continuous [CO] Datasets. High-resolution carbon monoxide (and methane) mixing ratios were determined for the Jurassic, Bryan Coast, and Dyer Plateau ice cores, West Antarctic Peninsula (Table 1 and *SI Appendix*, Fig. S1), via Continuous Flow Analysis (CFA) utilizing optical spectroscopy. Continuous [CO] for each core, integrated at 10-s intervals, are presented on a synchronized gas age scale in Fig. 1. The Full Width Half Maximum of gas age distributions, a common yardstick of achievable ice core temporal resolution, are 10 to 15 y and therefore on par with the seminal high-resolution Law Dome ice archive (38). Further details on the site characteristics, chronologies, and analytical methods are provided in *Materials and Methods* and *SI Appendix*.

As the longest record, Bryan Coast (1820 to 1981 CE; Fig. 1*B*) contributes most to our understanding of long-term trends. Data

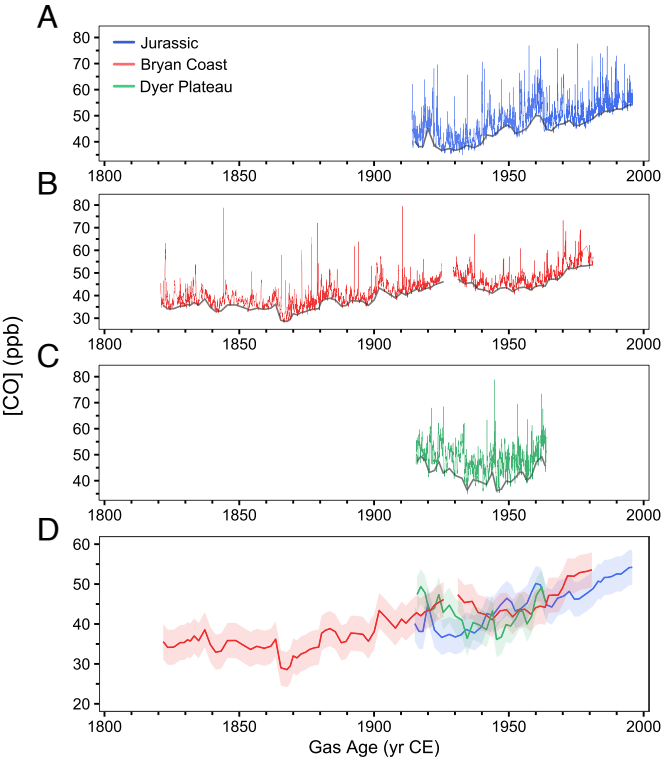

Fig. 1. Continuous ice core [CO] records. (*A*–*C*) 10-s integrated [CO] for Jurassic (blue), Bryan Coast (red), and Dyer Plateau (green), respectively. Baseline trends for each core are shown in gray and reproduced in (*D*) with corresponding colors for each core. Baseline [CO] records are defined as the fifth percentile of a 2-y moving window taken every 2 y and designed to resample the high-resolution datasets from only winter ice layers. Uncertainty envelopes are 2σ uncertainty on long-term reproducibility (*Materials and Methods*).

from Jurassic (1914 to 1995 CE; Fig. 1*A*) extends the ice core [CO] record into the direct observational era which begins in 1984 CE (39), and a short section of Dyer Plateau [CO] (1916 to 1964 CE; Fig. 1*C*) overlaps both cores to provide further replication. The Antarctic CO burden was roughly stable from 1820 to 1850 CE, decreased abruptly by ca. 5 ppb in 1865 CE before increasing toward a local maximum in 1925 CE (Fig. 1 *B* and *D*). From ca. 1925 to 1945 CE Bryan Coast and Dyer Plateau display a roughly bowl-shaped trend after which both records increase monotonically toward their youngest extents (Fig. 1 *B* and *C*). The CO mixing ratios recorded in the Jurassic core (Fig. 1*A*), however, are somewhat inconsistent with Bryan Coast and Dyer Plateau before 1945 CE. Between 1920 to 1930 CE, Jurassic [CO] is low despite both other records showing local maxima and then begins to increase almost 10 y earlier than recorded at both other sites. This inconsistency is best observed in the baseline [CO] trends displayed in Fig. 1*D*. While the records agree within uncertainty, the reason for an inconsistency in trends is currently unresolved. We note that excluding the Jurassic core does not significantly impact our final interpretation.

Superimposed on the multidecadal trends of all three datasets is a pervasive mode of high-frequency variability characterized by low amplitude (3 to 15 ppb) oscillations (Fig. 2) that are occasionally punctuated by high-amplitude, short-duration spikes of up to 40 ppb CO (Fig. 1). So far novel in Antarctic ice, a similar mode of variability has been well characterized in Greenland ice cores, albeit with a greater amplitude (40 to 80 ppb) (34, 40).

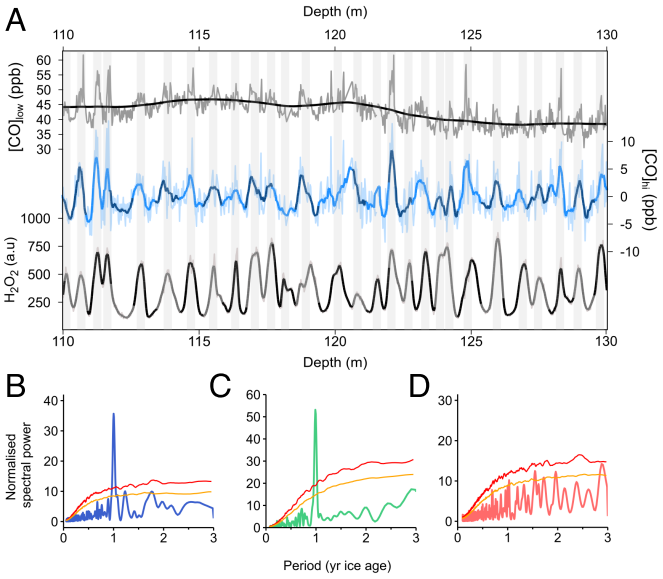

Fig. 2. Signal decomposition and spectral analysis. (*A*) Signal decomposition of high resolution [CO] across a typical depth section of Jurassic, compared with uncalibrated H_2O_2 measured simultaneously on the same CFA system. A 5 m moving average, taken twice ($[CO]_{low}$, black line) is subtracted from 10-s integrated CO data (gray) to produce residual CO ($[CO]_{hi}$, blue) before applying a 20 cm moving average. Gray-shaded vertical bars are H_2O_2 summer maxima. Alternate light and dark shading for $[CO]_{hi}$ and H_2O_2 shows depth-adjacent ice core sections. (*B–D*) Red-noise bias corrected Lomb–Scargle spectra calculated from $[CO]_{hi}$ across all analyzed depths for Jurassic (blue), Dyer Plateau (green), and Bryan Coast (red). Red and orange lines are 99% and 95% confidence, respectively, and indicate spectral power is above an AR1 process after 500 simulations of spectra with similar spectral characteristics.

Discussion—High-Frequency Variability

Implications of High-Frequency Variability for Atmospheric [CO] Reconstruction from Antarctic Ice. For Jurassic and Dyer Plateau, isolation of the high-frequency variability reveals residual CO maxima occur consistently in phase with Austral summer peaks in hydrogen peroxide (H_2O_2) (e.g., Fig. 2*A*), highlighting a quasi-annual component to the residual [CO] signal (Fig. 2 *B* and *C*). For Bryan Coast, the H_2O_2 signal itself is less well preserved and covariation between CO and H_2O_2 is also less robust (Fig. 2*D*), likely due to the lower snow accumulation rate at this site (Table 1).

Because the firn column acts as a low-pass filter of atmospheric variability, the observed quasi-annual signals cannot have an atmospheric origin (41). Highly reproducible measurements on parallel ice sticks also demonstrate that an analytical bias is not responsible (*SI Appendix*, Fig. S2). Instead, data are coherent with previously reported variability in Greenland ice that is thought to result from in situ CO production via the abiotic oxidation of organic matter occurring at some point below bubble close-off (34, 40). And it follows that these signals appear to be occurring in summer ice layers where concentrations of total organic carbon are typically higher than in winter layers (34, 42).

To remove the influence of in situ production on our atmospheric reconstruction, we adopt a baseline extraction technique following Faïn et al. (34), and resample our datasets from the lowest fifth percentile of a 2-y moving window (Fig. 1*D*). In doing so, each [CO] dataset is resampled from winter ice layers only and thus from depths where in situ production either does not occur or is negligible (e.g., 34, this work). A depth resolution <5 times the annual layer thickness of almost all the ice measured ensures that CO minima should always be resolved. Note that the firn-smoothing effect dictates that the bubbles in winter ice layers provide air samples that integrate across all seasons and multiple years. The records are then united as a multisite composite and combined 2σ uncertainty determined by propagating long-term reproducibility and core-specific calibration uncertainties (*Materials and Methods*).

The possibility for some ubiquitous background CO production means that records produced in this way are likely an upper limit for Antarctic [CO]. Nonetheless, because average baseline mixing ratios between 1825 to 1835 CE of 34 ± 4.8 ppb are statistically indistinguishable from the 35 ± 3.7 ppb [CO] reported by Faïn et al. (20)—who report no evidence of in situ production at their sites (Fig. 3*A*)—we are confident that any further influence of in situ production is negligible.

Discussion—Atmospheric Reconstruction

Connecting the Ice, Firn, and Flask Air Archives. Our multisite atmospheric CO reconstruction spans from 1821 to 1995 CE and is the first bubble-ice record of [CO] to overlap with direct atmospheric observations (Fig. 3). The Antarctic CO burden increases by ∼50% from a 35 ppb preindustrial level to a maximum of ca. 53 ppb in 1995 CE. Superimposed on this rise are two periods of multidecadal variability characterized by i) a minimum CO burden of ca. 30 in 1865 CE recorded in Bryan Coast and ii) a distinct plateau at around 41 ppb starting in 1920 CE that returns to growth by ca. 1945 CE. Growth rates on either side of the plateau in [CO] are 0.26 ppb CO y^{-1}.

The ca. 20 ppb preindustrial offset between continuous and discrete CO records (Fig. 3*A*) first observed by Faïn et al. (20) is reproduced. A decade-long overlap with direct flask air measurements from Mawson station, Antarctica (MAA; 39) support the accuracy of our measurements and allow us to strongly argue that earlier discrete CO analyses (15, 35) are compromised in some way, potentially by poorly constrained blanks, age uncertainty (20), and/or by aliasing of in situ production.

Notably, the local CO minimum in 1865 CE could not have been reproduced by Faïn et al. (20) due to the lower temporal resolution preserved at their ice core sites. The difference in trends around 1865 CE, therefore, likely relates to differences in

Table 1. Site locations

Core	Year drilled	Location	Elevation (m)	Depth interval (m)	Gas age interval (y CE)	Mean Δage (y)	Accumulation* (kg m^{-2} y^{-1})	−10 m Temp (°C)	Source
Jurassic	2012	74.1°S, 73.05°W	1,139	75.1 to 139.7	1914 to 1995	39	830	−16.7	(69, 70)
Bryan Coast	2011	74.50°S, 81.68°W	1,177	74.81 to 139.9	1820 to 1981	93	440	−23.4	(69)
Dyer Plateau	1988	70.68°S, 64.87°W	2,002	71.8 to 100.5	1916 to 1964	79	520	−21.0	(71)

*Average accumulation rate [a regional increase in snow accumulation has been observed since the turn of the 20th century (69)].

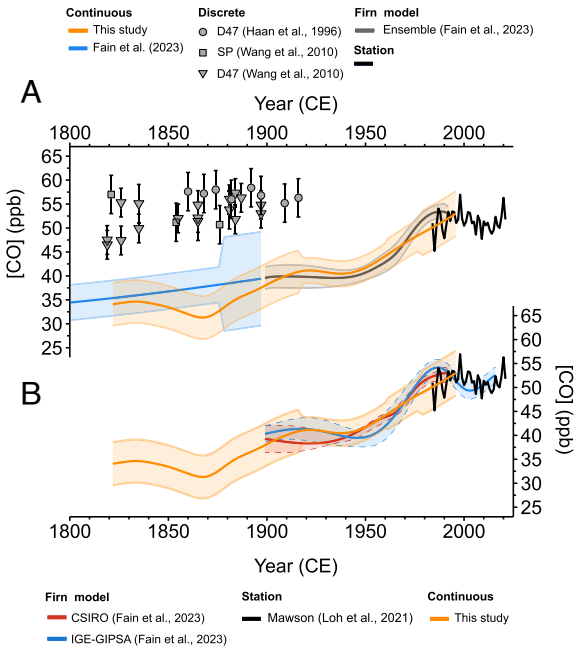

Fig. 3. Antarctic [CO] trends over the last 200 y. The new multisite composite baseline [CO] record (orange) is shown with a combined 2σ uncertainty envelope and smoothed to represent atmospheric trends. (*A*) Comparison to existing ice core (15, 20, 35), multimodel firn air (20) and direct Antarctic flask air observations from Mawson station (MAA, 1984-present; 39). (*B*) Comparison with multisite Antarctic firn air reconstructions (1898 to 2016; 20) produced using the IGE-GIPSA (blue, 43) and CSIRO (red, 44) inverse firn air transport models (20).

firn-based smoothing between the ice archives themselves. We note similar variability to observed here in fire-sensitive records of Antarctic refractory black carbon (6) and regional Southern Hemisphere sedimentary charcoal records (26).

In Fig. 3*B*, we also compare our record with the multisite Antarctic firn air inversions presented by Faïn et al. (20). Agreement between our ice core record and the firn air inversions support the fidelity of both reconstructions. This includes the observed plateau in [CO] growth, although the timings vary slightly between both inversions. After 1970 CE, both firn air reconstructions predict faster CO growth rates (0.4 ppb y^{-1}) than the ~0.26 ppb y^{-1} we report, and peak CO mixing ratios that occur ~6 y earlier than recorded at Mawson station (Fig. 3) suggesting that post-1970 CE, the firn air reconstructs may overestimate atmospheric CO growth rates. Overall, direct atmospheric observations that are more coherent with our ice archive than the firn air reconstructions support this hypothesis.

Comparison to AerChemMIP Simulations. A comparison of our new Antarctic [CO] record to a multimodel mean CO history from six state-of-the-art CCMs featured in the Aerosol Chemistry Model Intercomparison Project (AerChemMIP 12) reveals both similarities and notable differences (Fig. 4*B*). Over Antarctica (60 to 90°S), the modeled CO burden is consistent with the 50% increase observed from our ice core record and an acceleration in CO growth rate associated with rapid industrialization from 1950 CE. However, the AerChemMIP simulations do not record a 20th century period of stabilization, and absolute mean CO mixing ratios are generally overestimated relative to our reconstruction. The offset increases from a few percent to ca. 15% for the most recent three decades despite direct atmospheric measurements being available. Here, we investigate the possible factors driving the mismatch in variability between the AerChemMIP experiments and our ice core CO reconstruction.

First, since surface methane mixing ratios measured from ice cores are prescribed in all participating AerChemMIP models, CO production from CH_4-oxidation is well constrained and thus cannot be the source of slow-down in the CO growth rate. Second, modeling studies have repeatedly shown that [OH] was likely relatively stable prior to the 1980s (45, 46) and therefore changes in sink strength are also unlikely to be responsible. A well-reproduced increase in modeled OH abundance from 1980 CE (45, and references there in), however, invalidates an assumption of stable tropospheric [OH] for the most recent decades and as such we focus our discussion to pre-1980 CE. Finally, while differences in transport dynamics and chemical schemes are known to drive the large intermodel range in modeled CO burden (47) (1σ uncertainty in Fig. 4*B*), they do not drive a large diversity in modeled temporal trends (*SI Appendix*, Fig. S3). We must therefore assume that the direct CO emission inventories for biomass burning (BB4CMIP; 5) and/or anthropogenic activity (CEDS; 48) that support all AerChemMIP scenarios include inaccuracies or at least lack the detail to capture multidecadal trends.

According to the bottom–up CEDS inventory, direct emissions of Southern Hemisphere CO resulting from anthropogenic

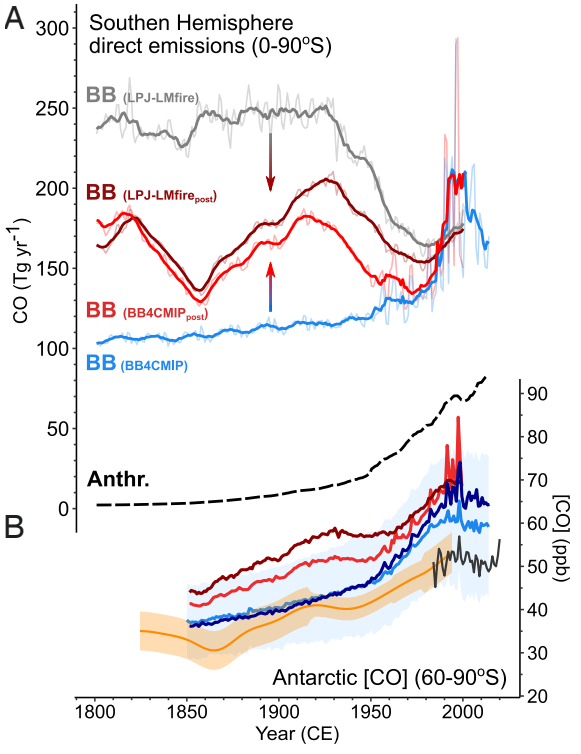

Fig. 4. Comparison of direct Southern Hemisphere CO emissions from select inventories with proxy and model reconstructions of the Antarctic CO burden. (*A*) Biomass burning (BB) emissions from BB4CMIP (blue, 5) and LPJ-LMfire (gray, 6) and their recently constrained (see arrows) counterparts BB4CMIP$_{post}$ (red) and LPJ-LMfire$_{post}$ (dark red) (53). Anthropogenic CEDS emissions (Anthr., dashed black) are from Hoesly et al. (48). Inventories are plotted as 2-y (faded color) and 10-y moving averages (bold color). (*B*) Data-Model comparison over 60 to 90°S. Observed carbon monoxide ratios are from this study (orange) and direct atmospheric observations from Mawson Station, Antarctica (black). Data are compared to a 6-model AerChemMIP mean with 1σ uncertainty (light blue), and box model output produced using different fire inventories: BB4CMIP (dark blue), BB4CMIP$_{post}$ (bright red) or LPJ-LMfire$_{post}$ (dark red). AerChemMIP outputs used in this work are from the CESM2- WACCM, GISS-E2-1-G, UKESM-0-LL, BCC-ESM1, GFDL-ESM4, and MRI-ESM2-0 models. Data can be accessed at: https://pcmdi.llnl.gov/CMIP6/.

fossil fuels and biofuel combustion increase slowly from ~3.4 Tg CO y^{-1} to 24.8 Tg CO y^{-1} between 1850 and 1950 CE, before almost tripling in the 50 y to 2000 CE (Fig. 4*A*). Here, a lack of emission rate variability across the first half of the 20th century is counter to globally significant events including two world wars and their associated economic downturn (48) and may potentially suppress variability in modeled [CO]. We know from ice cores, for example, that a reduction in CH_4 growth rate and a plateau in CO_2 mixing ratios occur between the 1920s and 1950s (38, 49) and could themselves be related to reduced human activity. Since CEDS emissions only represent a small fraction of total pre-1950 CE Southern Hemisphere CO emissions (Fig. 4*A* and *SI Appendix*, Fig. S4), it seems unlikely that an underestimation of variability could drive the observed mismatch between modeled and observed [CO]. If, however, the total magnitude of Southern Hemisphere anthropogenic CO emissions has been drastically underestimated, any uncertainties in CEDS emissions would be expected to have a greater impact, but there is currently little evidence to support such a scenario.

Potential Role of Southern Hemisphere Biomass Burning Variability. Unlike Southern Hemisphere CEDS emissions, divergent assumptions regarding the response of fire to human population growth and changes in land use (5, 6, 9, 10) allow for a wide range of potential paleofire histories over the past 200 y (2). The fire emissions inventory supporting AerChemMIP (12) and CMIP6 (11) simulations (BB4CMIP; 5), for example, utilize emissions outputs from six fire models that tend to scale up fire activity with human demographics at low to moderate population densities, giving rise to low preindustrial CO emissions that increase slowly toward 1950 CE (blue line, Fig. 4*A*). In contrast, population growth has been suggested to have had a negative impact on fire activity (e.g., 10), and Liu et al. (6) use the LPJ-LMfire global dynamic vegetation and fire model (50) to argue that Southern Hemisphere biomass burning was 30% higher in the preindustrial than in 2010 CE (gray line, Fig. 4*A*).

A 6-troposphere, 2-stratosphere box model is used to investigate the potential for Southern Hemisphere biomass-burning emissions to account for multidecadal variability observed in our ice core record. Model geometry and transport dynamics follow Mitchell et al. (51) but source/sink schemes have been updated, and tracer lifetimes explicitly simulated based on their atmospheric burden, known reaction rates, and imposed variations in OH (45), which vary with latitude and season (52) (*SI Appendix*). Atmospheric CO mixing ratios are then estimated as the balance between the sum of direct anthropogenic and biomass burning emissions, methane oxidation, and the oxidation of NMHCs resulting from anthropogenic, biomass burning, and biogenic sources, against the destruction of CO via reaction with OH (*SI Appendix*).

Utilizing the BB4CMIP fire inventory (here, our "standard" scenario), box model results over Antarctica (60 to 90°S; dark blue Fig. 4*B*) are consistent with the multimodel AerChemMIP output (light blue Fig. 4*B*), and both the temporal trends and slight positive bias relative to ice core and direct atmospheric observations are reproduced. The mean modeled global CO lifetime is 2.1 mo and total CO emissions between 1990 and 2000 CE are in line with previous literature ranges (*SI Appendix*, Fig. S4). A 20% change to tropical emissions produces a 1.5 ppb response over Antarctica (*SI Appendix*, Fig. S5) and due to its relatively short lifetime, CO mixing ratios are more sensitive to changes in extratropical emissions (30 to 60°S) than tropical emissions (0 to 30°S) by a factor of >3. Around 9.5 ppb of the total CO mixing ratio between 60 to 90°S is sourced from biomass burning originating from lower latitudes (*SI Appendix*, Fig. S4). This equates to roughly 25% of the total CO burden between 60 to 90°S in 1850 CE, declining to 18% by 2000 CE. Similarly, but using a variety of different Chemistry Transport Models (CTMs), Wang et al. (15) report 9.6 ppb of total [CO] at Scott Base, Antarctica (77°S), is sourced from biomass burning, Granier et al. (54) predict roughly 9 ppb at Syowa station (69°S) comes from wildfire, and Van der Werf et al. (4) predict a 7 ppb contribution from biomass burning at South Pole Station (90°S).

Assuming no changes to transport dynamics then additional variability in biomass burning, not currently expressed in the BB4CMIP dataset is required to reconcile the mismatch observed between the modeled and ice core–derived CO burden. Our model analysis (*SI Appendix*, Fig. S7) suggests that this would involve a decrease in Southern Hemisphere biomass burning emissions from the early 20th century of between 40 to 50% to counterbalance a simultaneous increase in anthropogenic emissions of both CO and CH_4.

Our results are corroborated by a recent study by Zhang et al. (53) in which gridded biomass burning emissions are derived from 1750 to 2010 CE by inversely constraining the existing BB4CMIP and LPJ-LMfire emissions datasets with a global array of ice core refractory black carbon (rBC) records. Interestingly, both inversions ($BB4CMIP_{post}$ and $LPJ\text{-}LMfire_{post}$; Fig. 4*A*) show similar trends irrespective of their start point to suggest that both prior inventories lie far from the ideal solution required to account for observed ice core rBC variability (53). Applying the $BB4CMIP_{post}$ and $LMfire_{post}$ emission scenarios in our box model, a plateau in Antarctic [CO] similar in timing and duration to that observed in the ice core record is reproduced (Fig. 4*B*). This provides independent proxy-constrained support to our hypothesis that the Southern Hemisphere may have experienced greater variability in biomass burning than currently predicted by the fire inventories used to force CMIP6 climate model simulations.

The timing of the CO plateau when using the inversions from Zhang et al. (53), however, occurs ca. 5 to 10 y later than observed in our ice core data, and the absolute CO burden is clearly overestimated. Age offsets are currently difficult to reconcile but could relate to chronological uncertainty—here between the Law Dome (55) and WD2014 (56) chronologies that both the [CO] and rBC records are tied to respectively. For the overestimated CO burden, explanations could involve the overestimation of CO emissions by Zhang et al. (53), an underestimation of sink strength, an overestimation of biogenic sources, or an overestimation of southward transport from the tropics but agreement between the "standard" box model and AerChemMIP outputs and sensitivity tests (*SI Appendix*), continue to suggest our box model is appropriate.

Finally, because CO has a relatively short lifetime, the spatial pattern of burning must also be considered (e.g., 19). Van der Werf et al. (4) have demonstrated with the TM5 CTM that CO from South American and Australian fires is more efficiently transported to Antarctica relative to CO from Southern Hemisphere Africa. Although, due to the greater magnitude of CO emissions from biomass burning across Southern Hemisphere Africa relative to South America, both contribute equally to the Antarctic CO burden (30% each), with Australia contributing only 11% (4). Zhang et al. (53) suggest most of the variability in their reconstructed emissions scenarios is driven by changes in fire activity across southern Africa with smaller contributions from southern South America and

Australia. However, as these inversions are tied to rBC, which has a shorter residence time than CO (residence time ~ 5 d), their reconstruction will express heightened sensitivity to extratropical fire activity. Although further spatial information cannot be extracted without a more complex atmospheric model, the fact that the two complementary methods agree, suggests a common, hemisphere-wide signal is driving features like the CO plateau.

Alternatively, a sustained change in the position of the Inter-Tropical Convergence Zone could alter the transport of CO from low Southern Hemisphere latitudes, changing the atmospheric burden above Antarctica without major changes in fire emissions. However, sedimentary charcoal records from the regions of interest provide strong evidence for a real change in fire activity, rather than a fully transport-driven scenario (26).

Drivers of Pre- to Post-industrial Southern Hemisphere Fire Activity. The observed period of [CO] stabilization between 1920 to 1950 CE falls counter to an assumption that scaling of paleofire activity with population growth held throughout the first half of the 20th century. Instead, a 20th century decline in biomass burning is now coherent across multiple models (e.g., 10, 57) and fire-proxy estimates from refractory black carbon-based inverse methods (53), Southern Hemisphere sedimentary charcoal records (26), and our new CO-based estimates.

Changes in both climate and land use could be responsible for the observed variability across our study period (7, 58) and both are thought to be important drivers of fire activity over the last millennium (e.g., 16). This said, Pechony and Shindell (57) have argued that a global reduction in fire emissions around the 1900s could not have occurred without human intervention. Similarly, the observed CO-plateau coincides with the most rapid rates of Southern Hemisphere land conversion for cropland and rangeland (59) that are well known to double as a form of passive fire suppression (1, 60, 61). We thus speculate that the period CO stabilization could be a key indicator of land-use change across the Southern Hemisphere—rapid expansion of land use for agriculture across Southern Hemisphere Africa, South America, and Australia (59, 62) effectively decoupling the relationship between fire activity and climate by the early 20th century (1, 7, 25, 57). Prior to 1920 CE, the increase in [CO] could also be due to land-use change, however, here associated with increasing biomass burning emissions under very low-density population growth (61) and initial land clearance—usually with fire—for agriculture (e.g., 63). Post-1950 CE, CO variability reflects the net result of multiple compounding factors and requires additional isotope and/or CCM analysis to deconvolve sources/sink dynamics.

Our multicore reconstruction of atmospheric CO reveals two periods of distinct multidecadal variability in the Southern Hemisphere CO burden since the preindustrial. Our analysis demonstrates that the stabilization of CO levels between 1920 to 1950 CE—not reproduced by state-of-the-art CCMs—can be satisfactorily explained by a reduction in Southern Hemisphere biomass burning rates, leading to a 40 to 50% decrease in CO emissions from 1920 CE until the late-20th century. Now supported by multiple lines of proxy-based evidence, we propose that unprecedented historical land use change across the Southern Hemisphere, associated with 20th century population growth, decreased biomass burning rates.

Materials and Methods

CFA. High-resolution trace gas analysis took place over three campaigns between Nov 2021 and Feb 2023 using the CFA system at the British Antarctic Survey (64), updated here to utilize optical-feedback cavity-enhanced absorption spectroscopy (*SI Appendix*, Fig. S9*A*; OF-CEAS 65, 66) for the simultaneous detection of CH_4 (67, 68), and low blank CO (34).

Briefly, ice core sticks were processed inside a T = −25 °C cold room, melted in succession on a heated melthead and pumped to the warm laboratory. Released gas bubbles were then separated from the continuous melt stream (ca. 10% air by volume) using a two-step extraction process. First, via a buoyancy-driven debubbler, and second, via a pressure gradient supplied across a gas-permeable membrane (Transfer-line degasser, Idex). A homemade Nafion dryer (TT-020, 0.3mm $Ø_{id}$, PermaPure) then dehumidified the sample before it was continuously injected into a laser spectrometer for analysis. Meanwhile, the degassed liquid fraction was directed to a broad spectrum of simultaneous chemical analyses, including the fluorometric detection of hydrogen peroxide (H_2O_2).

Continuous CO (and CH_4) measurements were obtained at an acquisition rate of 4 Hz using a Spectroscopy by Amplified Resonant Absorption (SARA) analyzer. Because the SARA has an effective cavity volume of only 0.24 cm^3 when maintained at 20 mbar, cavity renewal times of only 10 s are expected at standard ice core gas flow rates. Sample mixing in the optical cavity thus imparts negligible smoothing compared to that introduced by the geometry of the upstream CFA setup (e.g., 40). Specific operating conditions for each core are summarized in *SI Appendix*, Table S1.

Absolute Calibration. Sample underrecovery due to the inefficient extraction of dissolved gases (34, 67) was corrected for via a "Full Loop" calibration routine (68)–a method previously validated for both CO and CH_4 following comparison of discrete and continuous datasets from the same ice samples (34, 68).

Raw CFA data ($[CO]_{raw}$) were therefore translated to the WMOX-2014 reference scale and corrected for underrecovery of CO by bracketing each analysis run (consisting of ca. 6 h measurement time) with both dry gas and Full Loop ($[CO]_{fl}$) calibration routines. A Calibration Correction Factor (CCF) and Solubility Correction Factor (SCF) were then applied as daily averages using Eq. **1** and a 2.1 ppb procedural blank ($[CO]_{blk}$) determined via a single standard approach (34). Uncertainty on the blank assessment is assumed as 0.5 ppb and based on the relative magnitude of blank uncertainty from Faïn et al. (20). Before analysis, dynamic mixing experiments (*SI Appendix*, Fig. S9*B*; range 110 ppb to 0 ppb CO) between mass-flow controlled NOAA reference gases and ultrapure nitrogen (scrubbed for CO) confirmed the high linearity of the SARA analyzer ($R^2 = 0.9992$) with a negligible offset from origin and allow translation to WMOX-2014 reference scale using the day-to-day ratio of expected ($[CO]_{exp}$) to measured ($[CO]_{dry}$) concentration from a single NOAA-certified gas standard.

$$[CO]_{corr} = ([CO]_{raw} - [CO]_{blk}) \cdot SCF \cdot CCF, \quad \textbf{[1]}$$

where;

$$SCF = 1 + \frac{[CO]_{dry} - ([CO]_{fl} - [CO]_{blk})}{[CO]_{dry}} \quad \&, \quad CCF = \frac{[CO]_{dry}}{[CO]_{exp}}$$

Contamination of the air standard lines across three consecutive days of Bryan Coast analysis precluded daily corrections between 76.8 and 111.5 m depth (*SI Appendix*, Fig. S10). No correlated offset was observed for CH_4 and sample data bounding the contamination event were also internally consistent. We are confident that the contamination did not influence our measurements and likely originated from a microelectric switching valve that is isolated from the sample line (*SI Appendix*, Fig. S9*A*). In response, CCF and SCF values calculated from the unaffected analysis days to the impacted Bryan Coast depth range

Stability, Precision, and Accuracy. Allan Variance tests (72) were applied to Full Loop datasets from each campaign to characterize system stability and internal precision (67, 73). Optimal integration times were ca. 100 s for Jurassic and Bryan Coast, improving to >200 s for Dyer Plateau (*SI Appendix*, Fig. S9*C*). To balance precision and depth-resolution requirements, data presented here are averaged at 10-s intervals, yielding an internal precision (2*Allan deviation) of 1.2 ppb for Jurassic and Bryan Coast and 1.1 ppb for Dyer Plateau (2σ).

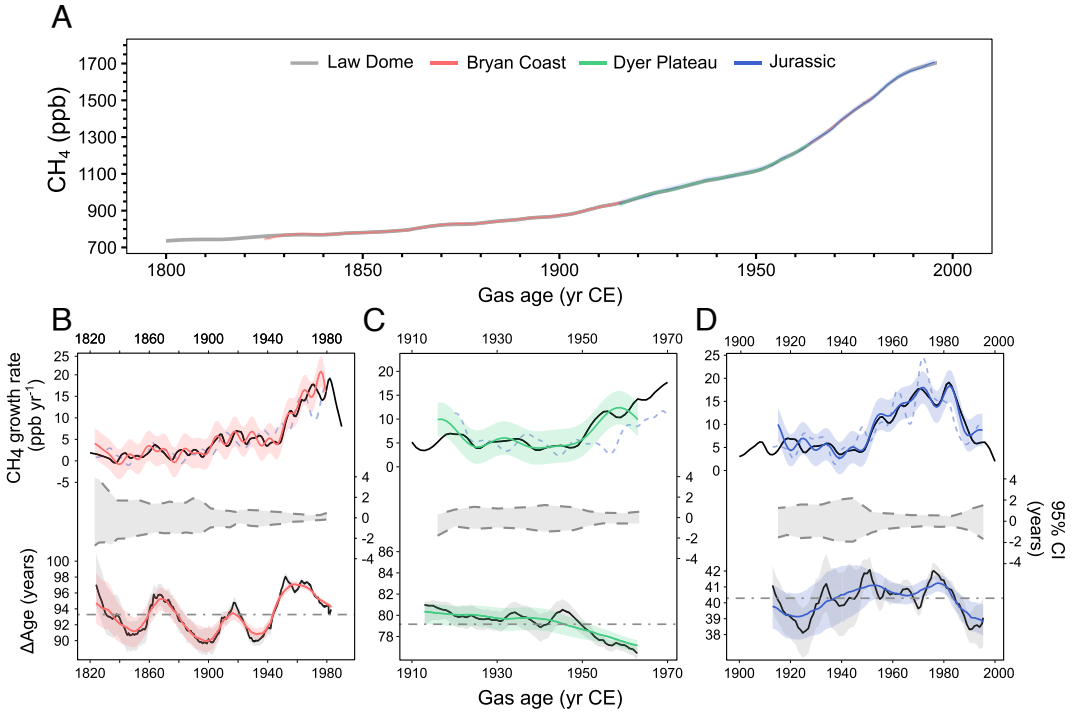

Fig. 5. MCMC gas age synchronization. (*A*) Posterior synchronizations for Bryan Coast (red), Dyer Plateau (green), and Jurassic (blue) compared to Law Dome ice and firn air target chronology (gray, 32). Overlapping core sections are obscured due to the goodness of fit to Law Dome CH_4 record. For each panel, (*B–D*); *Top*: 10-y band passed posterior CH_4 growth rates (bold color) compared with Law Dome (black). The dashed blue lines in each are growth rates calculated from initial age scales. *Middle*: 95% credibility intervals of posterior age model with respect to Law Dome. *Bottom*: posterior Δage (black) with 15-y moving average (bold color). Gray dashed lines show mean Δage.

Long-term reproducibility (external precision) was determined as 4.4 ppb (2σ) following analysis of replicate ice sticks, conducted a week apart, on a 7.5 m section of the Dyer core (*SI Appendix*, Fig. S2). Final reported accuracies represent the propagated 2σ uncertainty on Full Loop calibrations and external reproducibility along with an assumed 20% uncertainty on blank following the principles outlined in Tarantola (74).

System Resolution. Time-orientated data were transposed to the depth domain using smoothed melt rate histories recorded between core sections and the system lag between the ice core melting and signal detection (*SI Appendix*, Table S1). Data were then screened for contamination resulting from ambient air intrusion at core breaks using characteristically right-skewed spikes in methane concentration (ca. 1900 ppb) colocated with core breaks.

The extent of CFA-based signal smoothing was then investigated using the impulse response to a unit-step change in concentration under dynamic operating conditions i.e., sequentially melting ice sticks of different methane concentrations (ca. 350 vs. 600 ppb CH_4). Signal attenuation, or gain, was calculated following Stowasser et al. (67). At a melt rate of 5.5 cm min^{-1}, a depth resolution (50% cutoff) of 3.4 cm is achieved (*SI Appendix*, Fig. S11) which is several factors smaller than the Nyquist frequency required to theoretically resolve annual signals in almost all the ice analyzed.

Age Model. Preliminary gas age scales were constructed using ice age-gas age differences (Δage) predicted via the Oregon State University firn air transport model (75) with static Herron and Langway (76) densification physics. To facilitate the construction of a multisite record, comeasured CH_4 was then used to synchronize each chronology to that of Law Dome over the last 200 y (32, 55) using a Markov Chain Monte Carlo (MCMC) synchronization algorithm adapted from Muschitiello and Aquino-Lopez (77). A full description of the algorithm is provided in *SI Appendix*.

Synchronization results are shown in Fig. 5 and summarized in *SI Appendix*, Table S3. Each simulation was run for 1×10^6 iterations and the first 5×10^5 was discarded as burn-in to remove sensitivity to an arbitrary starting point before results were systematically thinned by 95% to limit autocorrelation. Convergence was monitored using a multivariate potential scale reduction factor <1.1 (78). The remaining 25,000 iterations were used to estimate the median synchronizations (Fig. 5*A*) and their 95% credibility intervals (*Middle* panel Fig. 5 *B–D*). A 15-y moving average was applied to modeled Δages before using them to produce our final age scales to accommodate for firn smoothing (*Bottom* panel Fig. 5 *B–D*). Age uncertainties relative to Law Dome are generally less than 2 y and remain ±4 y throughout.

Data, Materials, and Software Availability. The ice core data reported in this paper are available at https://doi.org/10.17863/CAM.109616 (79).

ACKNOWLEDGMENTS. This work was supported by the UK Natural Environment Research Council under grant NE/J020710/1 and by core funding from the British Antarctic Survey's Ice Dynamics and Paleoclimate Program. T.K.B. is supported by the Royal Society grant URF/R1/180366. F.M. acknowledges funding from a Natural Environment Research Council Discovery Science Grant (NE/W006243/1), and the support from the Isaac Newton Trust at the University of Cambridge (LCAG/444.G101121). P.L. and B.Z. acknowledge funding support from the Geosciences Directorate of the NSF under grant AGS-2102918. R.H.R. acknowledges funding from the Isaac Newton Trust at the University of Cambridge (LBZG/080.01.G101121). We thank Patricia Martinerie for useful discussions regarding firn modeling.

Author affiliations: [a]Department of Earth Sciences, University of Cambridge, Cambridge CB2 3EQ, United Kingdom; [b]British Antarctic Survey, Cambridge CB3 0ET, United Kingdom; [c]Université Grenoble Alpes, CNRS, Institut National de la Recherche Agronomique, Institut de Recherche pour le Développement, Grenoble Institut National du Patrimoine, Institut des Géosciences de l'Environnement, Grenoble 38000, France; [d]Department of Geography, University of Cambridge, Cambridge CB2 3EN, United Kingdom; [e]Centre for Climate Repair, Department of Applied Mathematics and Theoretical Physics, University of Cambridge, Cambridge CB3 0WA, United Kingdom; and [f]School of Earth and Atmospheric Sciences, Georgia Institute of Technology, Atlanta, GA 30332

1. D. M. Bowman *et al*., Fire in the earth system. *Science* **324**, 481–484 (2009).
2. F. Li *et al*., Historical (1700–2012) global multi-model estimates of the fire emissions from the Fire Modeling Intercomparison Project (FireMIP). *Atmos. Chem. Phys.* **19**, 12545–12567 (2019).
3. D. S. Hamilton *et al*., Reassessment of pre-industrial fire emissions strongly affects anthropogenic aerosol forcing. *Nat. Commun.* **9**, 3182 (2018).
4. G. Van der Werf, W. Peters, T. Van Leeuwen, L. Giglio, What could have caused pre-industrial biomass burning emissions to exceed current rates? *Clim. Past* **9**, 289–306 (2013).
5. M. J. Van Marle *et al*., Historic global biomass burning emissions for CMIP6 (BB4CMIP) based on merging satellite observations with proxies and fire models (1750–2015). *Geosci. Model Dev.* **10**, 3329–3357 (2017).
6. P. Liu *et al*., Improved estimates of preindustrial biomass burning reduce the magnitude of aerosol climate forcing in the Southern Hemisphere. *Sci. Adv.* **7**, eabc1379 (2021).
7. D. M. Bowman *et al*., Vegetation fires in the Anthropocene. *Nat. Rev. Earth Environ.* **1**, 500–515 (2020).
8. D. M. Bowman *et al*., The human dimension of fire regimes on Earth. *J. Biogeogr.* **38**, 2223–2236 (2011).
9. S. Hantson *et al*., The status and challenge of global fire modelling. *Biogeosciences* **13**, 3359–3375 (2016).
10. W. Knorr, L. Jiang, A. Arneth, Climate, CO_2 and human population impacts on global wildfire emissions. *Biogeosciences* **13**, 267–282 (2016).
11. V. Eyring *et al*., Overview of the coupled model intercomparison project phase 6 (cmip6) experimental design and organization. *Geosci. Model Dev.* **9**, 1937–1958 (2016).
12. W. J. Collins *et al*., AerchemMIP: Quantifying the effects of chemistry and aerosols in CMIP6. *Geosci. Model Dev.* **10**, 585–607 (2017).
13. D. Ferretti *et al*., Unexpected changes to the global methane budget over the past 2000 years. *science* **309**, 1714–1717 (2005).
14. J. A. Mischler *et al*., Carbon and hydrogen isotopic composition of methane over the last 1000 years. *Glob. Biogeochem. Cycles* **23**, GB4024 (2009).
15. Z. Wang, J. Chappellaz, K. Park, J. Mak, Large variations in southern hemisphere biomass burning during the last 650 years. *Science* **330**, 1663–1666 (2010).
16. C. J. Sapart *et al*., Natural and anthropogenic variations in methane sources during the past two millennia. *Nature* **490**, 85–88 (2012).
17. M. R. Nicewonger, M. Aydin, M. J. Prather, E. S. Saltzman, Large changes in biomass burning over the last millennium inferred from paleoatmospheric ethane in polar ice cores. *Proc. Natl. Acad. Sci. U.S.A.* **115**, 12413–12418 (2018).
18. M. R. Nicewonger, M. Aydin, M. J. Prather, E. S. Saltzman, Reconstruction of paleofire emissions over the past millennium from measurements of ice core acetylene. *Geophys. Res. Lett.* **47**, e2019GL085101 (2020).
19. M. R. Nicewonger, M. Aydin, M. J. Prather, E. S. Saltzman, Extracting a history of global fire emissions for the past millennium from ice core records of acetylene, ethane, and methane. *J. Geophys. Res. Atmos.* **125**, e2020JD032932 (2020).
20. X. Faïn *et al*., Southern hemisphere atmospheric history of carbon monoxide over the late Holocene reconstructed from multiple Antarctic ice archives. *Clim. Past Discuss.* **2023**, 1–38 (2023).
21. J. R. McConnell *et al*., 20th-century industrial black carbon emissions altered arctic climate forcing. *Science* **317**, 1381–1384 (2007).
22. J. R. McConnell *et al*., Hemispheric black carbon increase after the 13th-century māori arrival in New Zealand. *Nature* **598**, 82–85 (2021).
23. M. Legrand *et al*., Boreal fire records in northern hemisphere ice cores: A review. *Clim. Past* **12**, 2033–2059 (2016).
24. H. Bhattarai *et al*., Levoglucosan as a tracer of biomass burning: Recent progress and perspectives. *Atmos. Res.* **220**, 20–33 (2019).
25. J. R. Marlon *et al*., Climate and human influences on global biomass burning over the past two millennia. *Nat. Geosci.* **1**, 697–702 (2008).
26. J. R. Marlon *et al*., Reconstructions of biomass burning from sediment-charcoal records to improve data-model comparisons. *Biogeosciences* **13**, 3225–3244 (2016).
27. D. A. Falk *et al*., Multi-scale controls of historical forest-fire regimes: New insights from fire-scar networks. *Front. Ecol. Environ.* **9**, 446–454 (2011).
28. J. R. Marlon *et al*., Long-term perspective on wildfires in the Western USA. *Proc. Natl. Acad. Sci. U.S.A.* **109**, E535–E543 (2012).
29. M. O. Andreae, Emission of trace gases and aerosols from biomass burning-an updated assessment. *Atmos. Chem. Phys.* **19**, 8523–8546 (2019).
30. B. Duncan *et al*., Global budget of CO, 1988–1997: Source estimates and validation with a global model. *J. Geophys. Res. Atmos.* **112**, D22301-1–D22301-29 (2007).
31. B. Zheng *et al*., Global atmospheric carbon monoxide budget 2000–2017 inferred from multi-species atmospheric inversions. *Earth Syst. Sci. Data* **11**, 1411–1436 (2019).
32. C. Macfarling Meure *et al*., Law dome CO_2 CH_4 and NO_2 ice core records extended to 2000 years BP. *Geophy. Res. Lett.* **33**, L14810 (2006).
33. P. Novelli, K. Masarie, P. Lang, Distributions and recent changes of carbon monoxide in the lower troposphere. *J. Geophys. Res. Atmos.* **103**, 19015–19033 (1998).
34. X. Faïn *et al*., Northern Hemisphere atmospheric history of carbon monoxide since preindustrial times reconstructed from multiple Greenland ice cores. *Clim. Past* **18**, 631–647 (2022).
35. D. Haan, P. Martinerie, D. Raynaud, Ice core data of atmospheric carbon monoxide over Antarctica and Greenland during the last 200 years. *Geophys. Res. Lett.* **23**, 2235–2238 (1996).
36. S. Assonov *et al*., Evidence for a CO increase in the SH during the 20th century based on firn air samples from Berkner Island, Antarctica. *Atmos. Chem. Phys.* **7**, 295–308 (2007).
37. J. Schwander, B. Stauffer, Age difference between polar ice and the air trapped in its bubbles. *Nature* **311**, 45–47 (1984).
38. D. M. Etheridge, L. Steele, R. Francey, R. Langenfelds, Atmospheric methane between 1000 AD and present: Evidence of anthropogenic emissions and climatic variability. *J. Geophys. Res. Atmos.* **103**, 15979–15993 (1998).
39. L. R. Loh, Z., P. Krummel, Atmospheric CO at Mawson by commonwealth scientific and industrial research organisation, dataset published as co_maa_surface-flask_csiro_data1 at wdcgg, ver.2021-04-08-100. https://doi.org/10.50849/WDCGG_0016-7005-3001-01-02-9999. Accessed 11 February 2023.
40. X. Faïn *et al*., High resolution measurements of carbon monoxide along a late Holocene Greenland ice core: Evidence for in situ production. *Clim. Past* **10**, 987–1000 (2014).
41. C. Buizert, "Ice core methods | studies of firn air" in *Encyclopedia of Quaternary Science*, S. A. Elias, C. J. Mock Eds. (Elsevier, Amsterdam, ed. 2, 2013), pp. 361–372.
42. M. Legrand *et al*., Water-soluble organic carbon in snow and ice deposited at Alpine, Greenland, and Antarctic sites: A critical review of available data and their atmospheric relevance. *Clim. Past* **9**, 2195–2211 (2013).
43. E. Witrant *et al*., A new multi-gas constrained model of trace gas non-homogeneous transport in firn: Evaluation and behaviour at eleven polar sites. *Atmos. Chem. Phys.* **12**, 11465–11483 (2012).
44. C. Trudinger *et al*., Reconstructing atmospheric histories from measurements of air composition in firn. *J. Geophys. Res. Atmos.* **107**, ACH-15 (2002).
45. D. S. Stevenson *et al*., Trends in global tropospheric hydroxyl radical and methane lifetime since 1850 from AerChemMIP. *Atmos. Chem. Phys.* **20**, 12905–12920 (2020).
46. V. Naik *et al*., Preindustrial to present-day changes in tropospheric hydroxyl radical and methane lifetime from the Atmospheric Chemistry and Climate Model Intercomparison Project (ACCMIP). *Atmos. Chem. Phys.* **13**, 5277–5298 (2013).
47. D. Shindell *et al*., Multimodel simulations of carbon monoxide: Comparison with observations and projected near-future changes. *J. Geophys. Res. Atmos.* **111**, D19306 (2006).
48. R. M. Hoesly *et al*., Historical (1750–2014) anthropogenic emissions of reactive gases and aerosols from the Community Emissions Data System (CEDS). *Geosci. Model Dev.* **11**, 369–408 (2018).
49. D. M. Etheridge *et al*., Natural and anthropogenic changes in atmospheri CO_2 over the last 1000 years from air in Antarctic ice and firn. *J. Geophys. Res. Atmos.* **101**, 4115–4128 (1996).
50. M. Pfeiffer, A. Spessa, J. O. Kaplan, A model for global biomass burning in preindustrial time: LPJ-LMfire (v1. 0). *Geosci. Model Dev.* **6**, 643–685 (2013).
51. L. Mitchell, E. Brook, J. E. Lee, C. Buizert, T. Sowers, Constraints on the late Holocene anthropogenic contribution to the atmospheric methane budget. *Science* **342**, 964–966 (2013).
52. C. Spivakovsky *et al*., Three-dimensional climatological distribution of tropospheric OH: Update and evaluation. *J. Geophys. Res. Atmos.* **105**, 8931–8980 (2000).
53. B. Zhang *et al*., Improved biomass burning emissions from 1750 to 2010 using ice core records and inverse modeling. *Nat. Commun.* **15**, 3651 (2024).
54. C. Granier, G. Pétron, J. F. Müller, G. Brasseur, The impact of natural and anthropogenic hydrocarbons on the tropospheric budget of carbon monoxide. *Atmos. Environ.* **34**, 5255–5270 (2000).
55. M. Rubino *et al*., Revised records of atmospheric trace gases CO_2, CH_4,$N2_O$, and $\delta^{13}C$-CO_2 over the last 2000 years from Law Dome, Antarctica. *Earth Syst. Sci. Data* **11**, 473–492 (2019).
56. M. Sigl *et al*., The wais divide deep ice core wd2014 chronology-part 2: Annual-layer counting (0–31 ka bp). *Clim. Past* **12**, 769–786 (2016).
57. O. Pechony, D. T. Shindell, Driving forces of global wildfires over the past millennium and the forthcoming century. *Proc. Natl. Acad. Sci. U.S.A.* **107**, 19167–19170 (2010).
58. H. Wanner *et al*., Mid-to Late Holocene climate change: An overview. *Quat. Sci. Rev.* **27**, 1791–1828 (2008).
59. K. Klein Goldewijk, A. Beusen, J. Doelman, E. Stehfest, Anthropogenic land use estimates for the Holocene-HYDE 3.2. *Earth Syst. Sci. Data* **9**, 927–953 (2017).
60. S. Archibald, D. P. Roy, B. W. van Wilgen, R. J. Scholes, What limits fire? An examination of drivers of burnt area in Southern Africa *Glob. Chang. Biol.* **15**, 613–630 (2009).
61. W. Knorr, T. Kaminski, A. Arneth, U. Weber, Impact of human population density on fire frequency at the global scale. *Biogeosciences* **11**, 1085–1102 (2014).
62. N. Ramankutty, J. A. Foley, Estimating historical changes in global land cover: Croplands from 1700 to 1992. *Glob. Biogeochem. Cycles* **13**, 997–1027 (1999).
63. S. J. Pyne, *Fire: A Brief History* (University of Washington Press, 2019).
64. M. M. Grieman *et al*., Continuous flow analysis methods for sodium, magnesium and calcium detection in the Skytrain ice core. *J. Glaciol.* **68**, 90–100 (2022).
65. J. Morville, S. Kassi, M. Chenevier, D. Romanini, Fast, low-noise, mode-by-mode, cavity-enhanced absorption spectroscopy by diode-laser self-locking. *Appl. Phys. B* **80**, 1027–1038 (2005).
66. D. Romanini *et al*., Optical-feedback cavity-enhanced absorption: A compact spectrometer for real-time measurement of atmospheric methane. *Appl. Phys. B* **83**, 659–667 (2006).
67. C. Stowasser *et al*., Continuous measurements of methane mixing ratios from ice cores. *Atmos. Meas. Technol.* **5**, 999–1013 (2012).
68. R. H. Rhodes *et al*., Continuous methane measurements from a late Holocene Greenland ice core: Atmospheric and in-situ signals. *Earth Planet. Sci. Lett.* **368**, 9–19 (2013).
69. E. R. Thomas, J. S. Hosking, R. R. Tuckwell, R. Warren, E. Ludlow, Twentieth century increase in snowfall in coastal West Antarctica. *Geophys. Res. Lett.* **42**, 9387–9393 (2015).
70. B. D. Emanuelsson, E. R. Thomas, D. R. Tetzner, J. D. Humby, D. O. Vladimirova, Ice core chronologies from the antarctic peninsula: The Palmer, Jurassic, and Rendezvous age-scales. *Geosciences* **12**, 87 (2022).
71. L. G. Thompson *et al*., Climate since AD 1510 on Dyer Plateau, Antarctic Peninsula: Evidence for recent climate change. *Ann. Glaciol.* **20**, 420–426 (1994).
72. D. W. Allan, Statistics of atomic frequency standards. *Proc. IEEE* **54**, 221–230 (1966).
73. P. Werle, Accuracy and precision of laser spectrometers for trace gas sensing in the presence of optical fringes and atmospheric turbulence. *Appl. Phys. B* **102**, 313–329 (2011).
74. A. Tarantola, *Inverse Problem Theory and Methods for Model Parameter Estimation* (SIAM, 2005).
75. C. Buizert *et al*., Gas transport in firn: Multiple-tracer characterisation and model intercomparison for NEEM, Northern Greenland. *Atmos. Chem. Phys.* **12**, 4259–4277 (2012).
76. M. M. Herron, C. C. Langway, Firn densification: An empirical model. *J. Glaciol.* **25**, 373–385 (1980).
77. F. Muschitiello, M. A. Aquino-Lopez, Continuous synchronization of the Greenland ice-core and U-Th timescales using probabilistic inversion. *Clim. Past Discuss.* **2023**, 1–32 (2023).
78. S. P. Brooks, A. Gelman, General methods for monitoring convergence of iterative simulations. *J. Comput. Graph. Stat.*, 434–455 (1998).
79. R. Rhodes, I. Strawson, Data from "Antarctic ice core carbon monoxide records and composite spline 1821–1995 CE (Strawson et al., 2024)". Apollo - University of Cambridge Repository. https://doi.org/10.17863/CAM.109616. Deposited 6 June 2024.